photonics

MDPI

Article

Control of Multiphoton Excitation and Ionization Channels in Atoms Driven by Two-Color Femtosecond Laser Pulses

Shu-Qiao Li [1], Liang Xu [1,*], Jia-Hao Dong [1], Yi-Jia Mao [2], Xue-Min He [1], Zhao-Han Zhang [2], Hong-Bin Yao [3], Lu-Ning Li [4], Wei-Ming Xu [4] and Yi Liu [1]

[1] Shanghai Key Laboratory of Modern Optical System, University of Shanghai for Science and Technology, Shanghai 200093, China
[2] Key Laboratory for Laser Plasmas (Ministry of Education) and School of Physics and Astronomy, Collaborative innovation center of IFSA (CICIFSA), Shanghai Jiao Tong University, Shanghai 200240, China
[3] Key Laboratory of New Energy and Materials Research of Xinjiang Education Department, Xinjiang Institute of Engineering, Urumqi 830091, China
[4] Key Laboratory of Space Active Opto-Electronics Technology, Shanghai Institute of Technical Physics, Chinese Academy of Sciences, Shanghai 200083, China
* Correspondence: liangxu2021@usst.edu.cn

Abstract

By numerically solving the time-dependent Schrödinger equation (TDSE), we study the elementary excitation and ionization processes of atomic hydrogen on the same footing, which is irradiated by the two-color laser fields composed of a strong 400 nm pulse and a weak 800 nm pulse. We find that under different intensities of the 400 nm laser, the ionization and excitation probabilities exhibit completely distinct modulations with the variation in the intensity of the 800 nm laser. Electron energy spectra (EESs), including above-threshold ionization (ATI) peaks and below-threshold bound states, indicate that the involvement of Rydberg states and the shift of low-energy ATI peaks due to the increase in the ponderomotive energy are the primary causes of the above-mentioned modulation behavior. By virtue of a quantum-state-resolved numerical method, the angular-momentum-resolved EES reveal how the addition of the 800 nm laser field perturbs and modifies the strong, 400 nm dominated multiphoton excitation and ionization channels. Our study provides a flexible control strategy for multiphoton excitation and ionization in atoms and even molecules and further advances the understanding of the complex ultrafast dynamics driven by two-color femtosecond laser fields.

Keywords: above-threshold ionization; multiphoton excitation; angular-momentum-resolved electron energy spectra; quantum coherent control of atomic states

Check for updates

Received: 19 January 2026
Revised: 19 February 2026
Accepted: 25 February 2026
Published: 28 February 2026

1. Introduction

Laser-field-induced ionization is the initial stage of many ultrafast phenomena, such as molecular dissociation [1–4], high harmonic generation [5–8], terahertz radiation [9,10], air lasing [11–14], laser-assisted electron–ion recollision [15], and laser-induced plasma emission [16,17]. As such, it is a core issue in ultrafast laser physics and attosecond science. According to the Keldysh parameter γ [18], the ionization regime can be classified into multiphoton ($\gamma \gg 1$), tunneling ($\gamma \ll 1$), and over-the-barrier ionization processes. Among them, multiphoton ionization allows ionization channels to be clearly described using the concept of the number of absorbed photons, since the energy spacing of ATI peaks is equal to the single-photon energy of the driving light field. Thus, the multiphoton ionization picture remains a preferred choice for explaining related physical problems.

https://doi.org/10.3390/photonics13030236

Compared with photoionization, photoexcitation represents a more fundamental physical process in light–matter interactions. Semiclassical rate equations, the Fermi's Golden Rule, and the Jaynes–Cummings model were successively developed to quantitatively predict atomic single-photon transition probabilities [19,20]. However, with the advancement of high-power laser technology, multiphoton excitation has attracted considerable research interest. In this case, atomic energy levels are so severely distorted by laser fields that the aforementioned theoretical models are no longer applicable. At present, solving TDSE or density matrix equations is a preferable method to address this problem accurately [20,21].

Since the 1950s, the dependence of ionization probability on laser intensity in monochromatic fields has been extensively studied. A series of theoretical models were proposed [22–27], and all predicted that the ionization probability increased exponentially with light intensity, yet the excitation process was often neglected. However, this is not true, as excitation and ionization always coexist and interact with each other in intense laser fields. As early as 30 years ago, carefully detailed experiments observed that ion yields revealed minute yet reproducible modulations with small steps of intensity increment [28,29]. This phenomenon can be interpreted by the elaborate interference stabilization and channel closing models [30]. Then, C. D. Lin et al. theoretically studied antiphase modulations of excitation and ionization in atoms irradiated by lasers of different wavelengths based on EESs [31–33]. Subsequently, B. Piraux et al. used a quantum-state-resolved method to explain the probabilities of excitation and ionization driven by 800 nm and 1800 nm laser pulses from the perspectives of AC-Stark-shifted multiphoton resonance and frustrated ionization [34]. Recently, several joint experimental–theoretical studies on atomic excitation and ionization processes were performed from multiphoton to tunneling regime [35–37].

Compared to the monochromatic fields, a two-color field scheme composed of a fundamental wave and its second harmonic can provide more degrees of freedom to optimize the ultrafast electron dynamics. For example, both the total ionization probability and the asymmetry of electron emission can be controlled via parallel two-color fields [38,39]. The electronic intercycle and intracycle interferences of different electron wave packets are disentangled by using orthogonally polarized two-color fields [40,41]. However, these studies all overlook the contribution from excited states, which play a key role in interpreting the frustrated ionization and below-threshold harmonic generation [42,43]. Thus, there is an urgent need for a complete description of atomic electron behavior under two-color fields.

Lately, a simultaneous study of two-color-field-driven excitation and ionization dynamics was reported [44]. They confirmed that ionization reduction in atoms independent of the relative phase between two-color laser fields is induced by the modification of excitation channels. Furthermore, the modulation of ionization and excitation probabilities by the relative phase was investigated based on the interference between different channels [45]. In addition to the relative phase, the relative intensity between the two-color components also serves as an important control parameter for atomic excitation and ionization. Nevertheless, the relevant control strategies have rarely been reported and the excitation dynamics remain to be investigated.

In this paper, we carry out TDSE calculations to study atomic excitation and ionization on an equal footing driven by two-color laser fields with wavelengths of 400 nm and 800 nm over a wide intensity range. We focus mainly on 800 nm light-intensity-dependent excitation and ionization probabilities, and attempt to reveal the underlying physical mechanisms. Firstly, we find that under different 400 nm laser intensities, atomic ionization and excitation probabilities show completely distinct changes with the 800 nm intensity. Then, based on multiphoton ionization picture, the EES containing bound states is used to intuitively explain the reasons for the modulation of ionization and excitation. More importantly, the spherical harmonics expansion method adopted for solving TDSE makes it possible to resolve quantum states of bound and ionized wave packets. On this basis, it is revealed how the multiphoton excitation and ionization channels of atoms vary with different laser intensities.

The rest of this paper is organized as follows. In Section 2, a short summary of numerical model and method used for solving TDSE will be described. In Section 3, simulation results are discussed, and the corresponding channels of excitation and ionization are revealed clearly. Section 4 presents a summary and outlook of our findings.

2. Numerical Models and Methods

The interaction between atoms and femtosecond laser pulses can be described by TDSE within the electric dipole approximation, which is written as (atomic units are used in this article unless otherwise indicated):

$$i\frac{\partial}{\partial t}\Psi(\boldsymbol{r},t) = [-\frac{\nabla^2}{2} + V(r) - i\boldsymbol{A}(t)\cdot\nabla]\Psi(\boldsymbol{r},t), \tag{1}$$

where the velocity gauge is adopted, $\Psi(\mathbf{r},t)$ is the total wave function of the system including both bound and ionized states, $V(r) = -1/r$ is the Coulomb potential of the hydrogen atom, and ∇ and ∇^2, respectively, are the spatial nabla and Laplace operators. The collinearly polarized laser vector potential $\boldsymbol{A}(t)$ is defined as follows:

$$\boldsymbol{A}(t) = f(t)\left[-\frac{E_{400}}{\omega_{400}}\sin(\omega_{400}t) - \frac{E_{800}}{\omega_{800}}\sin(\omega_{800}t)\right]\vec{e}, \tag{2}$$

where $\omega_{400/800}$ denotes the angular frequency of 400 or 800 nm laser fields, $f(t) = \sin^2(\pi t/T_p)$ is a laser pulse envelope with a duration of $T_p = 10T_{800}$, and $T_{800} = 2\pi/\omega_{800}$. $\vec{e}$ is a unit vector along the z-axis. The initial phase difference between the two-color fields is set to zero. $E_{400/800}$ denotes the peak amplitude of 400 nm or 800 nm laser pulses, which is related to laser intensity via $E = \sqrt{I/(3.51\times10^{16})}$ with I in unit of $\mathrm{W/cm^2}$. In our simulations, the 400 nm laser intensity I_{400} varies from 5.0×10^{13} $\mathrm{W/cm^2}$ to 1.5×10^{14} $\mathrm{W/cm^2}$, and I_{800} is scanned from 0 to 8.0×10^{12} $\mathrm{W/cm^2}$.

To trace excitation and ionization channels in atoms driven by intense laser pulses, TDSE is solved using angular momentum eigenstate expansion method. The time-dependent total wave function consists of B-spline functions and spherical harmonics:

$$\Psi(r,\theta,\varphi,t) = \sum_{j,l} c_{jl}(t)\frac{B_j(r)}{r}Y_{lm}(\theta,\varphi). \tag{3}$$

where $B_j(r)$ denotes B-spline functions and $Y_{lm}(\theta,\varphi)$ are spherical harmonics with orbital angular momentum quantum number l and magnetic quantum number m, which, respectively, describe electronic radial and angular dynamics. The time-dependent $c_{jl}(t)$ are undetermined expansion coefficients, and their initial value is obtained by diagonalizing the field-free Hamiltonian. For collinearly polarized laser fields, magnetic quantum number m is conserved. Thus, to accelerate numerical simulations, m is fixed as 0 since the hydrogen atom is initially populated at the ground electronic state $n = 1$, $l = 0$, and $m = 0$, where n is the principal quantum number. j and l are both integers ranging from zero to $N_r - 1$ and from zero to $N_l - 1$, where N_r and N_l denote the numbers of B-spline functions and l partial waves, respectively. n satisfies the following equation $n = j + l + 1$. Detailed information about this numerical method can be found in Ref. [46].

At the end of the laser pulses ($t = t_f$), the quantum-state-resolved probability is extracted using the projection method:

$$P_{nl} = |\langle \psi_{nl}(\boldsymbol{r}) \mid \Psi(\boldsymbol{r}, t_f) \rangle|^2, \tag{4}$$

where $\psi_{nl}(\boldsymbol{r})$ denotes the eigenstates of the hydrogen atom with an energy eigenvalue E_{nl}, and $\Psi(\boldsymbol{r}, t_f)$ is the final-state wave function of the system. The remaining probability for the ground state is given by $P^g = P_{n=1,l=0}$. Then, the total excitation probability P^e excluding the ground state is obtained by $P^e = \sum_{nl} P_{n>1,l}$. Thus, the ionization probability is obtained by $P^i = 1 - P^g - P^e$ since the total probability of the system's wave function is normalized to unity.

The photoelectron energy spectra (PESs) are very useful for analyzing the ionization channels. In analogy with Equation (4), the PESs can be calculated by projecting the final wave function onto scattering states:

$$P^i(\varepsilon) = \sqrt{2\varepsilon} \int |\langle \Phi^-_{\boldsymbol{k}}(\boldsymbol{r}) \mid \Psi(t_f) \rangle|^2 d\Omega_k, \tag{5}$$

where $\Phi^-_{\boldsymbol{k}}(\boldsymbol{r})$ is the electronic scattering state with the outgoing momentum $\boldsymbol{k} = (k, \Omega_k)$. k and Ω_k refer, respectively, to the magnitude and direction of momentum, and the former corresponds the electronic kinetic energy via $\varepsilon = k^2/2$. Alternatively, $P^i(\varepsilon)$ is the summation of the populations of all l partial waves, and thus, the l-resolved energy spectra can be obtained by:

$$P^i_l(\varepsilon) = 2\sqrt{2}\varepsilon^{3/2} Z^2_l(k), \tag{6}$$

where $Z_l(k)$ is the l partial wave projection with a given momentum k [46].

In analogy with the PESs in continuum, the energy density in bound states is instructive to consider excitation and ionization on the same footing by defining $P(\varepsilon) = (\sum_l P_{nl})n^3$. Note that a hydrogen atom with the energy $\varepsilon = -1/(2n^2)$ has n-fold degeneracy for given (n, $m = 0$) quantum numbers. Here, our EESs contain both the above-threshold ionization peaks and energy density distribution of bound states.

Equation (1) is solved in a spherical space with a radius $r_{\max} = 1500$ a.u., which is large enough to retain all ionized wave packets. The converged results are obtained with $N_l = 40$, 1500 B-spline functions, and time step $\Delta t = 0.008$ a.u. That means n ranges from 1 to 41 and l ranges from 0 to $n - 1$. Therefore, a total of 861 bound states are taken into account in our numerical simulations.

3. Results and Discussions

Figure 1a,b show, respectively, the ionization and excitation probabilities in hydrogen atoms irradiated by bichromatic fields composed of 400 nm and 800 nm laser pulses. The y- and x-axes correspond to the laser intensities at 400 nm and 800 nm, respectively. As expected, the atomic ionization probability rapidly increases with increasing 400 nm laser intensity in Figure 1a because I_{400} is one order of magnitude higher than I_{800}. However, for a given I_{400}, the ionized atoms do not increase monotonically with the 800 nm laser intensity, especially for the low 400 nm intensity case indicated by the red dashed line. In contrast to the ionization case, the excitation phenomena display completely different behaviors in Figure 1b. The excitation probability always reaches a maximum near $I_{800} = 2.0 \times 10^{12}$ W/cm^2 when I_{400} is lower than 1.0×10^{14} W/cm^2, as encircled by green dashed lines. However, when I_{400} becomes higher, the excitation minima always appear around the same 800 nm peak intensity of 2.0×10^{12} W/cm^2, as indicated by yellow dotted lines.

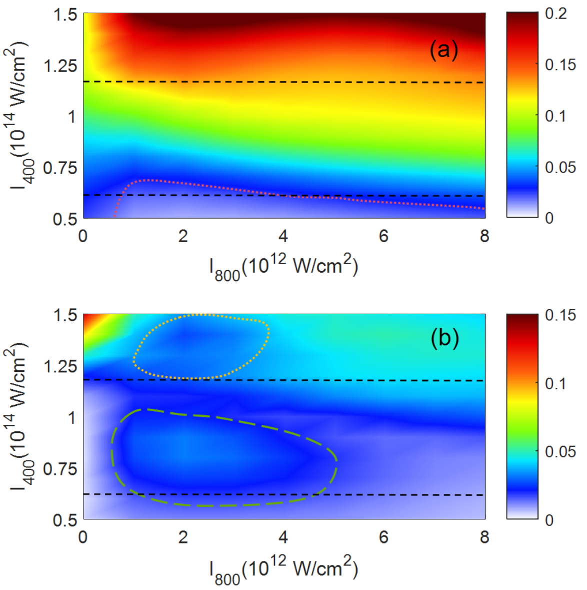

Figure 1. Dependence of the ionization (**a**) and excitation probabilities (**b**) in hydrogen atoms, on the laser intensities I_{400} and I_{800}. Both laser pulses are linearly polarized and have a duration of $10T_{800}$ with phase difference $\phi = 0$. The data marked by horizontal dashed lines correspond to Figure 2.

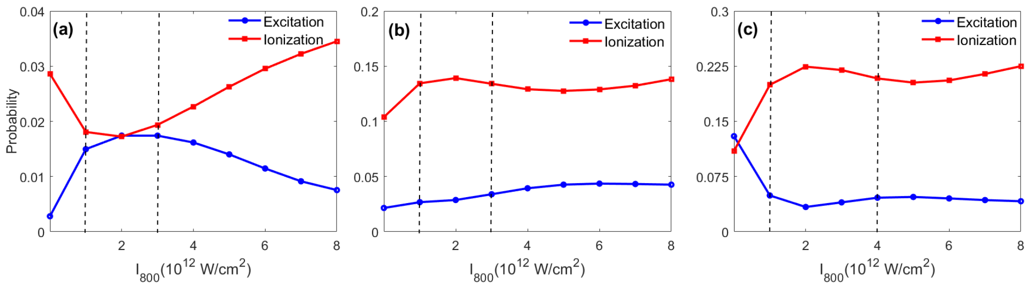

Figure 2. The ionization (red lines) and excitation (blue lines) probabilities of hydrogen atoms as a function of I_{800}. The 400 nm laser intensities are fixed at 6×10^{13} W/cm^2 in (**a**), 1.2×10^{14} W/cm^2 in (**b**), and 1.5×10^{14} W/cm^2 in (**c**). Other laser parameters are the same as those used in Figure 1. The data marked by vertical dashed lines in panels (**a**), (**b**), and (**c**) correspond to Figures 3, 4, and 5, respectively.

To clarify the changes in ionization and excitation probabilities, we extract three typical results (marked by horizontal dashed lines) from Figure 1, as shown in Figure 2. Panels (a), (b), and (c), respectively, correspond to $I_{400} = 6 \times 10^{13}$, 1.2×10^{14}, and 1.5×10^{14} W/cm^2. As can be seen, ionization and excitation probabilities exhibit distinct trends with varying I_{800} for different 400 nm laser intensities. In Figure 2a, the ionized probability first decrease and then increase, while the excitation probability shows an initial increase followed by a decrease. This anticorrelation phenomenon is similar to the reports in previous research [32,44]. In contrast, in Figure 2c, the ionization yield first increases and then remains nearly constant and the excitation probability initially decreases and then shows no significant variation. Moreover, the excitation probability in panel (c) is much larger than those in panels (a) and (b). In Figure 2b, the ionization yield exhibits a similar variation trend to that in Figure 2c. However, the population in the excited states shows a slow continuous increase.

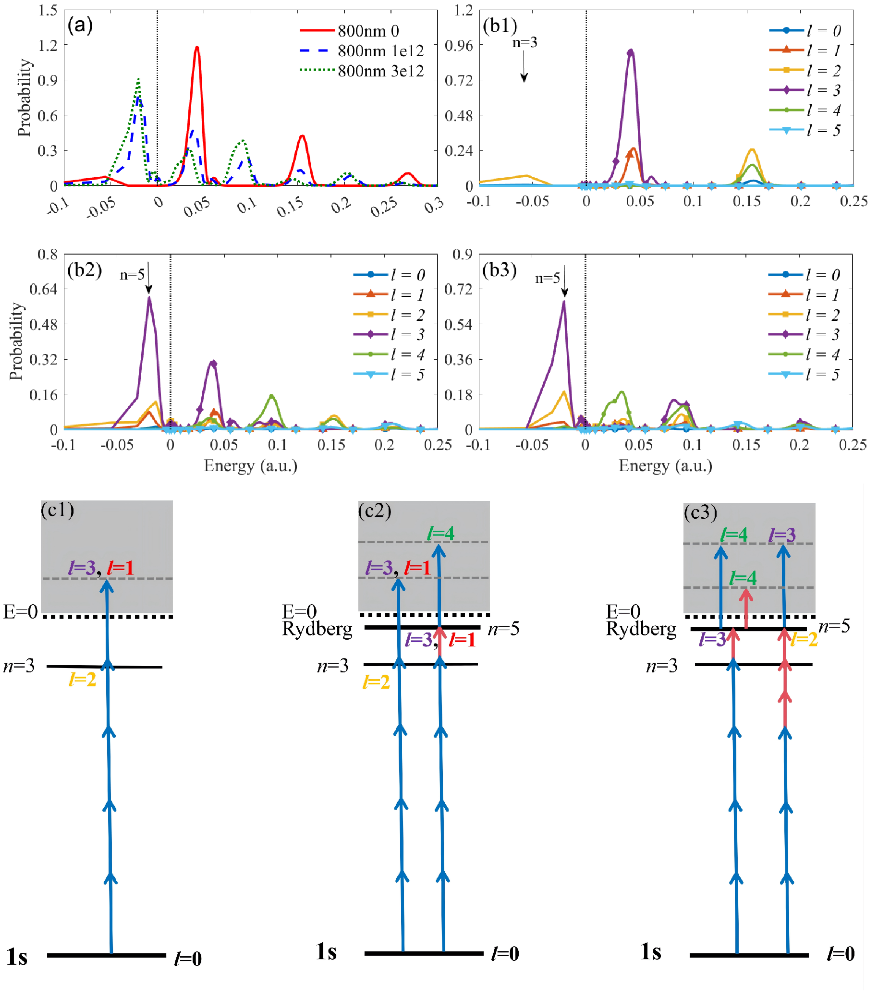

Figure 3. (**a**) The EESs including bound and ionized states at different 800 nm intensities. The 400 nm intensity is fixed at I_{400} = 6 × 10^{13} W/cm^2. The red solid, blue dashed, and green dotted lines, respectively, correspond to I_{800} = 0, 1 × 10^{12}, and 3 × 10^{12} W/cm^2. (**b1**), (**b2**), and (**b3**) are the angular-momentum-resolved EESs for the red solid, blue dashed, and green dotted lines in (**a**), respectively. The l-resolved ionization and excitation channels (**c1**), (**c2**), and (**c3**) correspond to (**b1**), (**b2**), and (**b3**), respectively. Note that only the main channels are labeled. For clarity, angular momentum labels in (**c1**–**c3**) are assigned the same colors as the respective peaks shown in (**b1**–**b3**). The same applies below.

Varying the relative intensity of the two-color fields can affect atomic ionization and excitation processes, thereby controlling its ultrafast dynamics. Next, we will investigate the excitation and ionization channels from the perspective of multiphoton absorption. We first analyze Figure 2a. For a fixed 400 nm intensity of 6 × 10^{13} W/cm^2, we calculate the EESs including bound and ionized states at different 800 nm intensities, as shown in Figure 3a. When the 800 nm laser field is turned off, there exists a set of typical ATI peaks with energy intervals of ω_{400}, as represented by the red solid line. The corresponding angular momentum-resolved EESs in Figure 3(b1) shows the population of bound states is mainly concentrated in the energy level with $n = 3$, and $l = 2$; the first ATI peak includes the partial waves with l = 3 and 1, while the second one mainly consists of the components with l = 2 and 4. Notably, the peak for l = 3 is much higher than others. Next, we will explain the origin of this angular momentum distribution.

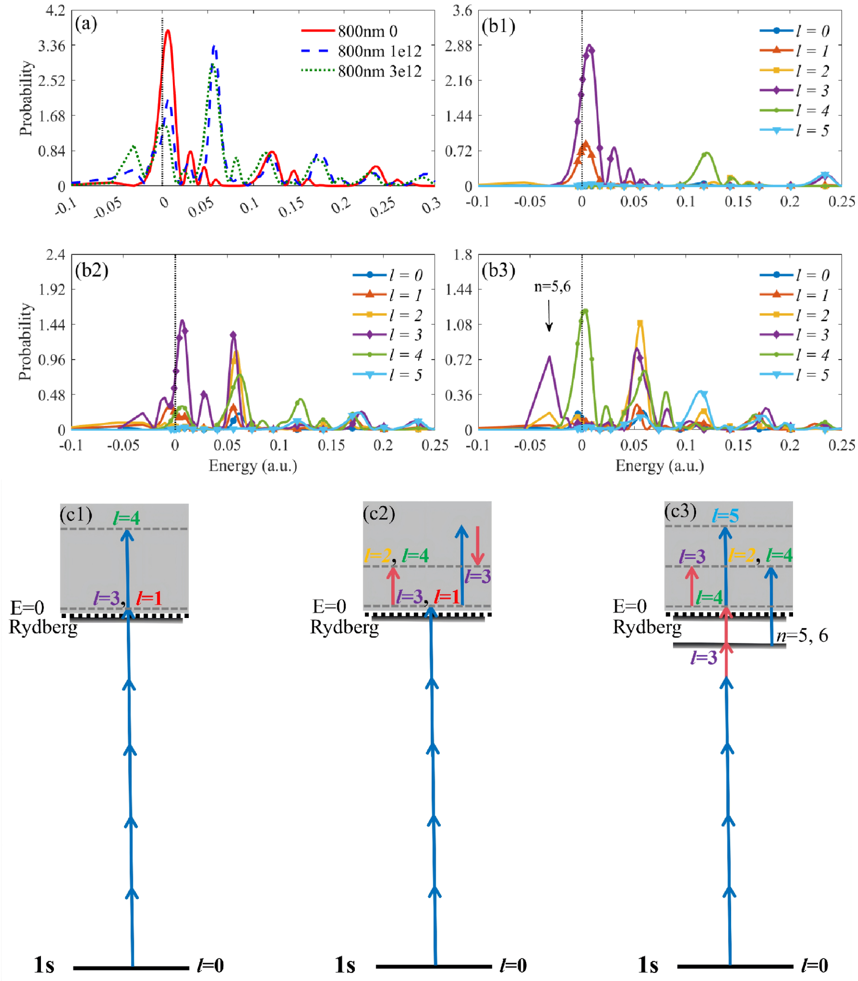

Figure 4. (**a**) The EESs at different 800 nm intensities, and I_{400} is fixed at 1.2×10^{14} W/cm^2. The red solid, blue dashed, and green dotted lines, respectively, correspond to I_{800} = 0, 1×10^{12}, and 3×10^{12} W/cm^2. (**b1**), (**b2**), and (**b3**) are the l-resolved EESs for the red solid, blue dashed, and green dotted lines in (**a**), respectively. (**c1**), (**c2**), and (**c3**) are transition channels for (**b1**), (**b2**), and (**b3**), respectively.

According to the transition selection rule, when an atom absorbs a photon, the parities of its initial and final states must be opposite, and its angular momentum must satisfy $\Delta l = \pm 1$ [47,48]. As such, if a ground-state hydrogen atom absorbs an even (odd) number of photons, its angular momentum will become even (odd). Here, ground-state atoms first absorb four 400 nm photons to reach the resonant energy level with $n = 3$. According to the aforementioned transition rules, only the sublevels with $l = 0$ and 2 can be populated. However, the $l = 2$ partial wave dominates over the $l = 0$ component because atoms prefer to transition to a state with a larger angular momentum [36,49], as shown by the blue ($l = 0$, $n = 3$) and yellow ($l = 2$, $n = 3$) lines in Figure 3(b1). Subsequently, these atoms with $l = 2$ absorb an additional 400 nm photon and are ionized, forming the ATI peaks with $l = 1$ and 3. Similarly, the latter is far greater than the former because of its larger l value. These processes are described by Figure 3(c1).

Once an 800 nm laser pulse is added, the ATI peaks induced by the 400 nm laser decline obviously, and the below-threshold population increases significantly and is mainly distributed at energy levels with $n = 5$ just below $\varepsilon = 0$ a.u., as depicted by blue lines in Figure 3a, which leads to a reduction in ionization and an increase in excitation, further implying the involvement of Rydberg states. Meanwhile, a new set of ATI peaks with ω_{400} energy difference emerges.

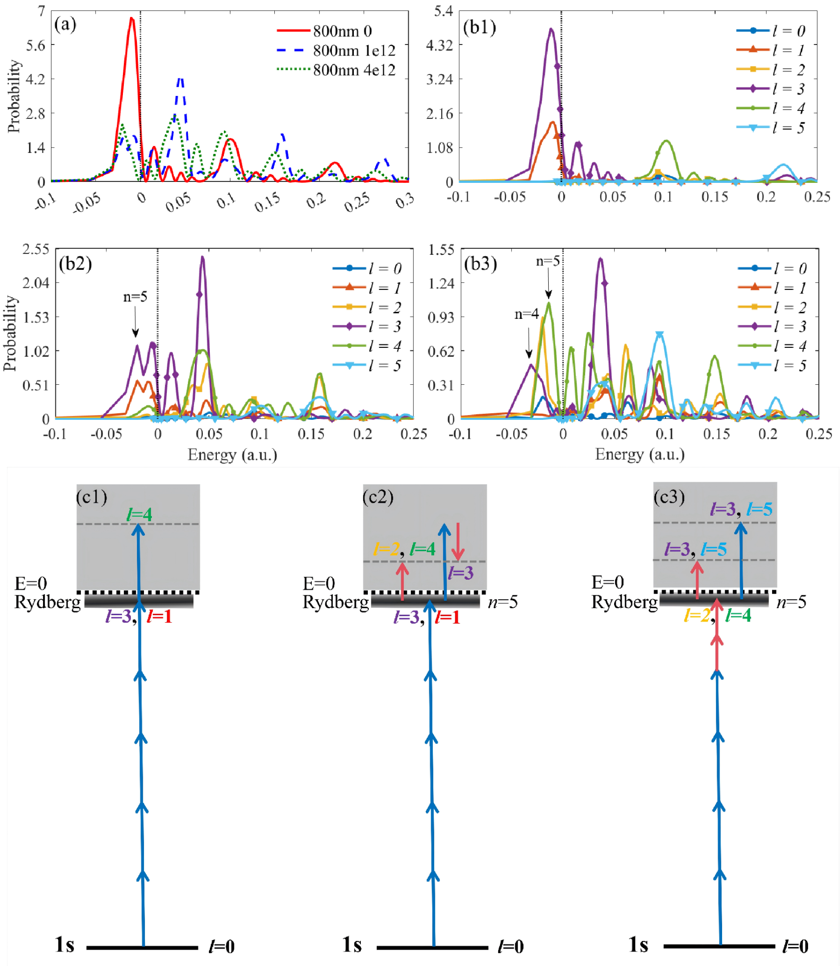

Figure 5. (**a**) The EESs at different 800 nm intensities, and I_{400} is fixed at 1.5×10^{14} W/cm^2. The red solid, blue dashed, and green dotted lines, respectively, correspond to I_{800} = 0, 1×10^{12}, and 4×10^{12} W/cm^2. (**b1**), (**b2**), and (**b3**) are the *l*-resolved EESs for the red solid, blue dashed, and green dotted lines in (**a**), respectively. The transition channels (**c1**), (**c2**), and (**c3**) correspond to (**b1**), (**b2**), and (**b3**), respectively.

How are the Rydberg states and new peaks formed? Figure 3(b2) shows the *l*-resolved EESs. The below-threshold peaks are mainly distributed at l = 3, 2, and 1. Since the energy gap between the states with n = 5 and 3 is approximately equal to ω_{800}, it can be deduced that the ground-state atoms undergo an excitation process of $4\omega_{400} + \omega_{800}$ to reach these Rydberg states. Although Rydberg states are relatively hard to be ionized due to their quasi-bound state properties [32,33,44], they can still absorb a ω_{400} photon to be ionized, giving rise to a new peak with l = 4, as indicated by the green line near ε = 0.1 a.u. in Figure 3(b2). Figure 3(c2) depicts the corresponding quantum-state-resolved transition channels. In principle, the electron in the ground state could also first absorb five 400 nm photons and then one 800 nm photon to reach this l = 4 peak. However, our analysis of quantum-state-resolved populations does not support this scenario, so the probability of this process is extremely low.

Next, we analyze the transition channels of Figure 2b. If I_{400} increases to 1.2×10^{14} W/cm^2, the total number of EESs changes significantly, as shown in Figure 4a. The typical 400 nm-dominated ATI peaks exhibit an enhanced yield and move entirely to lower energies due to an increase in the ionization threshold induced by a considerable ponderomotive energy

$U_p \approx 0.066$ a.u. Thus, the multiphoton-resonant transition to the n = 3 excited states no longer occurs. Notably, nearly half of the first ATI peak has become bound states, indicating that the formation of Rydberg states no longer requires the participation of the 800 nm component in this case. Figure 4(b1) presents the corresponding l-dependent EES. By adding an 800 nm pulse with 1×10^{12} W/cm^2, another significant peak emerges near ε = 0.05 a.u. and consists of partial waves with l = 2, 3, and 4, as shown in Figure 4(b2). The peaks with l = 2 and 4 are formed via the absorption of an additional 800 nm photon by the l = 3 partial wave of the first 400 nm-dominated ATI peak. The same energy peak with l = 3 can be produced via absorbing six 400 nm photons followed by emitting one 800 nm photon, i.e., the $6\omega_{400}$–ω_{800} process. These specific transition channels are labeled in Figure 4(c1,c2).

When I_{800} increases to 3×10^{12} W/cm^2, the angular momenta l of the initial 400 nm ATI peaks exhibit remarkable changes, as shown in Figure 4(b3). l varies from 3 to 4 for the peak spanning the zero energy, and from 4 to 5 for the one with energy close to 0.1 a.u. Additionally, a significant number of highly excited Rydberg states (n = 5 and 6) are populated, as shown by the purple line with l = 3 near $\varepsilon = -0.025$ a.u., which leads to a slow increase of the total excitation probability in Figure 2b. These Rydberg states are directly populated via $4\omega_{400} + \omega_{800}$ transition process without intermediate states, then become the ATI peak with l = 4 at the zero energy point by subsequently absorbing ω_{800}. This peak with l = 4 cannot only absorb ω_{800} again to form the ionization peak with l = 3 around $\varepsilon = 0.05$ a.u., but also produce the peak with l = 5 near $\varepsilon = 0.1$ a.u. via absorbing a 400 nm photon. Certainly, the Rydberg states can also be ionized by absorbing a 400 nm photon, generating the l = 2 and 4 partial waves in the continuum. The relevant channels are summarized in Figure 4(c3).

Finally, we analyze Figure 2c, which corresponds to $I_{400} = 1.5 \times 10^{14}$ W/cm^2. In this case, the multiphoton picture is still applicable since the Keldysh parameter γ is approximately equal to 1.75 and the ponderomotive energy U_p equals 0.082 a.u. The actual ionization energy rises to 0.582 a.u., which implies that the hydrogen atom cannot be ionized by absorbing five 400 nm photons. Therefore, the peak induced by the 400 nm five-photon process dives below the ionization threshold due to a larger ponderomotive shift, as shown in Figure 5a, leading to the formation of a large number of Rydberg states. The corresponding l-resolved distributions in Figure 5(b1) are almost identical to those in Figure 4(b1).

When the 800 nm pulse with an intensity of 1×10^{12} W/cm^2 is introduced, the number of ATI peaks increases significantly, as indicated by the blue dashed line in Figure 5a. Figure 5(b2) reveals that the increase in ionization probability is due to the depletion of more Rydberg states. In other words, these Rydberg states with l = 3 and 1 can form the ionization peaks with l = 4 and 2 by absorbing an 800 nm photon. Interestingly, the ATI peak with $l = 4$ near $\varepsilon = 0.1$ a.u. disappears because it evolves into the $l = 3$ partial wave with a lower energy near 0.05 a.u. by emitting an 800 nm photon. These ionization partial waves at $\varepsilon \approx 0.05$ a.u. can continue to absorb a photon with energy ω_{400} to form the ionization peaks with l = 2, 4, and 5 near ε = 0.15 a.u. These related transition channels are depicted in Figure 5(c1,c2).

When I_{800} increases to 4×10^{12} W/cm^2, the EESs in Figure 5(b3) become more complex. The Rydberg states with l = 2 and 4 are formed via a $4\omega_{400} + 2\omega_{800}$ transition process. They can absorb another photon with energy ω_{800} or ω_{400} to produce the l = 3 and 5 partial waves near $\varepsilon = 0.025$ a.u. or 0.1 a.u. This ATI peak with l = 3 can continue to absorb ω_{800} or ω_{400} to reach the l = 4 ionization peak near $\varepsilon =$ 0.1 a.u. or 0.15 a.u. Because the 800 nm laser is involved in both excitation and ionization, a dynamic equilibrium between them can be achieved. Thus, the ionization and excitation probabilities remain essentially constant in

Figure 2c when I_{800} exceeds 4×10^{12} W/cm^2. These transition channels are illustrated in Figure 5(c3).

4. Conclusions and Outlooks

In this paper, we investigate the multiphoton excitation and ionization of atomic hydrogen in a dichromatic field composed of 400 nm and 800 nm lasers by numerically solving the three-dimensional TDSE. Based on the multiphoton ionization picture, we carefully analyze the effects of laser intensity variations on ionization and excitation via the evolution of EESs. Furthermore, using the quantum-state-resolved numerical method, we clearly reveal how the transition channels are tuned by varying the intensities of the two-color fields: the intense 400 nm laser determines the dominant excitation and ionization channels, while the weak 800 nm laser component perturbs these dominant channels. Depending on the intensity of the 400 nm fields, we identify three typical scenarios with distinct characteristics.

When the 400 nm laser is relatively weak, the four-photon resonant excitation and further five-photon ionization arise simultaneously. The population in excited states is intercepted to the Rydberg states by the introduced 800 nm laser, leading to a decrease in ionization probability and an increase in excitation yield. With a further increase in the intensity of the 800 nm laser field, the Rydberg states are depleted, thereby leading to a subsequent increase in ionization and a decrease in excitation probabilities.

If the 400 nm laser is further increased up to 1.2×10^{14} W/cm^2, the EES peaks shift toward lower energies such that the first ATI peak is centered at the ionization threshold, directly generating high-lying Rydberg states. Then, the addition of an 800 nm laser depletes this ATI peak, forming a series of new peaks in the continuum. If the intensity of the 800 nm laser is further increased, some new channels emerge, such as $4\omega_{400} + \omega_{800}$ and $4\omega_{400} + 2\omega_{800}$ processes.

When the intensity of the 400 nm laser pulses reaches 1.5×10^{14} W/cm^2, the original first ionization peak becomes fully converted into bound states due to an increase in ponderomotive energy, resulting in a higher excitation probability. These bound states are ionized by a newly introduced 800 nm laser. Consequently, with increasing the intensity of the 800 nm laser pulse, the ionization probability increases, while the excitation probability decreases. With a further increase in the intensity of the 800 nm laser, the 800 nm component participates in both excitation and ionization via various processes, such as $4\omega_{400} + 2\omega_{800}$, $4\omega_{400} + 3\omega_{800}$, and $4\omega_{400} + 2\omega_{800} + \omega_{400}$. A balance between ionization and excitation makes excitation and ionization probabilities keep basically constant as I_{800} increases.

In summary, by continuously tuning the intensity ratio of the two-color laser pulses, we can control the multiphoton excitation and ionization channels of hydrogen atoms, thereby modifying their ionization and excitation probabilities. In addition to the intensity ratio, the relative phase of the two-color field is another key control parameter. Although adjusting this phase does not change the transition channels, it still modifies the transition probability due to quantum interference effects [45]. Thus, the phase-control method serves as an excellent complement to the intensity-based control approach. Their combination enables precise control over strong-field excitation and ionization. In principle, these strategies are also applicable to other atomic and molecular systems, and can be extended to other wavelength combinations. Our research has promising applications in strong-field laser physics, including optimizing the high-order harmonic generation and the terahertz radiation, as well as enhancing the preparation of Rydberg states. Our studies could also help improve the quality of femtosecond laser-induced breakdown spectroscopy data, thus offering potential for hydrogen detection in future planetary exploration (e.g., searching for life traces in Mars exploration [16]).

Author Contributions: Conceptualization, L.X., H.-B.Y. and Y.L.; methodology, S.-Q.L., Y.-J.M., L.-N.L. and Z.-H.Z.; software, H.-B.Y. and Z.-H.Z.; validation, S.-Q.L., J.-H.D. and Y.-J.M.; formal analysis, S.-Q.L., L.X. and Y.L.; investigation, S.-Q.L., J.-H.D. and L.X.; data curation, S.-Q.L. and J.-H.D.; writing—original draft preparation, S.-Q.L. and L.X.; writing—review and editing, H.-B.Y., L.-N.L., W.-M.X. and Y.L.; visualization, S.-Q.L., L.X. and X.-M.H.; supervision, L.X. and Y.L.; project administration, L.X. and Y.L.; funding acquisition, L.X., H.-B.Y., L.-N.L. and Y.L. All authors have read and agreed to the published version of the manuscript.

Funding: This research was supported by the National Natural Science Foundation of China (NSFC) (Grant No. 12574379, 12595341, 12595342, 62475273, and 12474283), Shanghai Rising Star Program (Grant No. 23QA1411000), Tianshan Talent Training Program of Xinjiang (Grant No. 2023TSYCJU0009) and Natural Science Foundation of Xinjiang Uygur Autonomous Region (Grant No. 2025D01E19).

Data Availability Statement: Data underlying the results presented in this paper are not publicly available at this time but may be obtained from the authors upon reasonable request.

Acknowledgments: The authors are grateful to Feng He for the helpful and enlightening discussions.

Conflicts of Interest: The authors declare no conflicts of interest.

References

1. Giusti-Suzor, A.; Mies, F.H.; DiMauro, L.F.; Charron, E.; Yang, B. Dynamics of H_2^+ in intense laser fields. *J. Phys. B At. Mol. Opt. Phys.* **1995**, *28*, 309–339. [CrossRef]
2. Kling, M.F.; Siedschlag, C.; Verhoef, A.J.; Khan, J.I.; Schultze, M.; Uphues, T.; Ni, Y.; Uiberacker, M.; Drescher, M.; Krausz, F.; et al. Control of Electron Localization in Molecular Dissociation. *Science* **2006**, *312*, 246–248. [CrossRef] [PubMed]
3. He, F.; Ruiz, C.; Becker, A. Control of Electron Excitation and Localization in the Dissociation of H_2^+ and Its Isotopes Using Two Sequential Ultrashort Laser Pulses. *Phys. Rev. Lett.* **2007**, *99*, 083002. [CrossRef] [PubMed]
4. Kunitski, M.; Eicke, N.; Huber, P.; Köhler, J.; Zeller, S.; Voigtsberger, J.; Schlott, N.; Henrichs, K.; Sann, H.; Trinter F.; et al. Double-slit photoelectron interference in strong-field ionization of the neon dimer. *Nat. Commun.* **2019**, *10*, 1. [CrossRef]
5. McPherson, A.; Gibson, G.; Jara, H.; Johann, U.; Luk, T.S.; McIntyre, I.A.; Boyer, K.; Rhodes, C.K. Studies of multiphoton production of vacuum-ultraviolet radiation in the rare gases. *J. Opt. Soc. Am. B* **1987**, *4*, 595–601. [CrossRef]
6. Ferray, M.; L'Huillier, A.; Li, X.F.; Lompre, L.A.; Mainfray, G.; Manus, C. Multiple-harmonic conversion of 1064 nm radiation in rare gases. *J. Phys. B At. Mol. Opt. Phys.* **1988**, *21*, L31–L35. [CrossRef]
7. Krause, J.L.; Schafer, K.J.; Kulander, K.C. High-order harmonic generation from atoms and ions in the high intensity regime. *Phys. Rev. Lett.* **1992**, *68*, 3535–3538. [CrossRef]
8. Corkum, P.B. Plasma perspective on strong field multiphoton ionization. *Phys. Rev. Lett.* **1993**, *71*, 1994–1997. [CrossRef]
9. Hamster, H.; Sullivan, A.; Gordon, S.; White, W.; Falcone, R.W. Subpicosecond electromagnetic pulses from intense laser-plasma interaction. *Phys. Rev. Lett.* **1993**, *71*, 2725–2728. [CrossRef]
10. Xie, X.; Dai, J.; Zhang, X.-C. Coherent Control of THz Wave Generation in Ambient Air. *Phys. Rev. Lett.* **2006**, *96*, 075005. [CrossRef]
11. Luo, Q.; Liu, W.; Chin, S.L. Lasing action in air induced by ultra-fast laser filamentation. *Appl. Phys. B* **2003**, *76*, 337–340. [CrossRef]
12. Dogariu, A.; Michael, J.B.; Scully, M.O.; Miles, R.B. High-Gain Backward Lasing in Air. *Science* **2011**, *331*, 442–445. [CrossRef] [PubMed]
13. Yao, J.; Zeng, B.; Xu, H.; Li, G.; Chu, W.; Ni, J.; Zhang, H.; Chin, S.L.; Cheng, Y.; Xu, Z. High-brightness switchable multiwavelength remote laser in air. *Phys. Rev. A* **2011**, *84*, 051802(R). [CrossRef]
14. Zhang, X.; Lu, Q.; Zhu, Y.; Zhao, J.; Danylo, R.; Xu, L.; Lei, M.; Jiang, H.; Wu, C.; Zhang, Z.; et al. Multiple-photon resonance enabled quantum interference in emission spectroscopy of N_2^+. *Ultrafast Sci.* **2024**, *4*, 0051. [CrossRef]
15. Xu, J.-L.; Blaga, C.I.; DiChiara, A.D.; Sistrunk, E.; Zhang, K.-K.; Chen, Z.-J.; Le, A.-T.; Morishita, T.; Lin, C.-D.; Agostini, P.; et al. Laser-Induced Electron Diffraction for Probing Rare Gas Atoms. *Phys. Rev. Lett.* **2012**, *109*, 233002. [CrossRef]
16. Li, L.; Liu, X.; Xu, W.; Wang, J.; Shu, R. A laser-induced breakdown spectroscopy multi-component quantitative analytical method based on a deep convolutional neural network. *Spectrochim. Acta B* **2020**, *169*, 105850. [CrossRef]
17. Guo, J.; Zhang, Z.; Zhang, N.; Shang, B.; Xue, J.; Wang, Y.; Tao, S.; Xie, B.; Guo, L.; Lin, L.; et al. Sub-ppb NaCl aerosol detection at a distance of 30 meters by femtosecond laser induced plasma spectroscopy. *Opt. Express* **2023**, *31*, 28586–28595. [CrossRef]
18. Keldysh, L.V. Ionization in the Field of a Strong Electromagnetic Wave. *Sov. Phys. JETP* **1965**, *20*, 1307.

19. Rabi, I.I. On the Process of Space Quantization. *Phys. Rev.* **1936**, *49*, 324. [CrossRef]
20. Scully, M.O.; Zubairy, M.S. *Quantum Optics*; Cambridge University Press: Cambridge, UK, 1997.
21. Bachau, H.; Cormier, E.; Decleva, P.; Hansen, J.E.; Martín, F. Applications of B-splines in atomic and molecular physics. *Rep. Prog. Phys.* **2001**, *64*, 1815. [CrossRef]
22. Landau, L.D.; Lifshits, E.M. *Quantum Mechanics: Nonrelativistic Theory*, 3rd ed.; Pergamon: Oxford, UK, 1997
23. Perelomov, A.M.; Popov, V.S.; Terent'ev, M.V. Ionization of Atoms in an Alternating Electric Field. *Sov. Phys. JETP* **1966**, *23*, 924–934.
24. Perelomov, A.M.; Popov, V.S.; Terent'ev, M.V. Ionization of Atoms in an Alternating Electric Field, I.I. *Sov. Phys. JETP* **1967**, *24*, 207–217.
25. Perelomov, A.M.; Popov, V.S.; Terent'ev, M.V. Ionization of Atoms in an Alternating Electric Field, I.I.I. *Sov. Phys. JETP* **1967**, *25*, 336–343.
26. Bauer, D.; Mulser, P. Exact field ionization rates in the barrier-suppression regime from numerical time-dependent Schroinger-equation calculations. *Phys. Rev. A* **1999**, *59*, 569–577.
27. Tong, X.M.; Zhao, Z.X.; Lin, C.D. Theory of molecular tunneling ionization. *Phys. Rev. A* **2002**, *66*, 033402. [CrossRef]
28. Talebpour, A.; Chien, C.Y.; Chin, S.L. Population trapping in rare gases. *J. Phys. B At. Mol. Opt. Phys.* **1996**, *29*, 5725–5733. [CrossRef]
29. Talebpour, A.; Liang, Y.; Chin, S.L. Population trapping in the CO molecule. *J. Phys. B At. Mol. Opt. Phys.* **1996**, *29*, 3435–3442. [CrossRef]
30. Fedorov, M.; Movsesian, A. Field-induced effects of narrowing of photoelectron spectra and stabilisation of Rydberg atoms. *J. Phys. B At. Mol. Opt. Phys.* **1988**, *21*, L155–L158.
31. Morishita, T.; Lin, C.D. Photoelectron spectra and high Rydberg states of lithium generated by intense lasers in the over-the-barrier ionization regime. *Phys. Rev. A* **2013**, *87*, 063405. [CrossRef]
32. Li, Q.; Tong, X.-M.; Morishita, T.; Wei, H.; Lin, C.D. Fine structures in the intensity dependence of excitation and ionization probabilities of hydrogen atoms in intense 800-nm laser pulses. *Phys. Rev. A* **2014**, *89*, 023421. [CrossRef]
33. Li, Q.; Tong, X.-M.; Morishita, T.; Jin, C.; Wei, H.; Lin, C.D. Rydberg states in the strong field ionization of hydrogen by 800, 1200 and 1600 nm lasers. *J. Phys. B At. Mol. Opt. Phys.* **2014**, *47*, 3435–3442. [CrossRef]
34. Piraux, B.; Mota-Furtado, F.; O'Mahony, P.F.; Galstyan, A.; Popov Yu, V. Excitation of Rydberg wave packets in the tunneling regime. *Phys. Rev. A* **2017**, *96*, 043403. [CrossRef]
35. Xu, S.; Liu, M.; Hu, S.; Shu, Z.; Quan, W.; Xiao, Z.; Zhou, Y.; Wei, M.; Zhao, M.; Sun, R.; et al. Observation of a transition in the dynamics of strong-field atomic excitation. *Phys. Rev. A* **2020**, *102*, 043104. [CrossRef]
36. Chetty, D.; Glover, R.D.; deHarak, B.A.; Tong, X.M.; Xu, H.; Pauly, T.; Smith, N.; Hamilton, K.R.; Bartschat, K.; Ziegel, J.P.; et al. Observation of dynamic Stark resonances in strong-field excitation. *Phys. Rev. A* **2020**, *101*, 053402. [CrossRef]
37. Chetty, D.; Glover, R.D.; Tong, X.M.; deHarak, B.A.; Xu, H.; Haram, N.; Bartschat, K.; Palmer, A.J.; Luiten, A.N.; Light, P.S.; et al. Carrier-Envelope Phase-Dependent Strong-Field Excitation. *Phys. Rev. Lett.* **2022**, *128*, 173201. [CrossRef]
38. Schafer, K.J.; Kulander K.C. Phase-dependent effects in multiphoton ionization induced by a laser field and its second harmonic. *Phys. Rev. A* **1992**, *45*, 8026. [CrossRef]
39. Paulus, G.G.; Becker, W.; Walther, H. Classical rescattering effects in two-color above-threshold ionization. *Phys. Rev. A* **1995**, *52*, 4043. [CrossRef]
40. Skruszewicz, S.; Tiggesbäumker, J.; Meiwes-Broer, K.-H.; Arbeiter, M.; Fennel, T.; Bauer, D. Two-Color Strong-Field Photoelectron Spectroscopy and the Phase of the Phase. *Phys. Rev. Lett.* **2015**, *115*, 043001. [CrossRef]
41. Zipp, L.J.; Natan, A.; Bucksbaum, P.H. Probing electron delays in above-threshold ionization. *Optica* **2014**, *1*, 361. [CrossRef]
42. Li, M.; Qin, L.; Wu, C.; Peng, L.; Gong, Q.; Liu, Y. Rescattering and frustrated tunneling ionization of atoms in circularly polarized laser fields. *Phys. Rev. A* **2014**, *89*, 013422. [CrossRef]
43. Xiong, W.; Geng, J.; Tang, J.; Peng, L.; Gong, Q. Mechanisms of Below-Threshold Harmonic Generation in Atoms. *Phys. Rev. Lett.* **2014**, *112*, 233001. [CrossRef]
44. Yao, H.-B.; Qu, Q.-W.; Zhang, Z.-H.; Wang, J.-W.; Gao, J.; Hu, C.-X.; Li, H.; Wu, J.; He, F. Multiphoton Ionization Reduction of Atoms in Two-Color Femtosecond Laser Fields. *Phys. Rev. Lett.* **2023**, *130*, 113201. [CrossRef]
45. Yao, H.-B.; Zhang, Z.-H.; Hu, C.-X.; He, F. Multiphoton excitation and ionization of hydrogen atoms in two-color laser fields. *Phys. Rev. A* **2023**, *108*, 043112. [CrossRef]
46. Zhang, Z.-H.; Li, Y.; Mao, Y.-J.; He, F. QPC-TDSE: A parallel TDSE solver for atoms and small molecules in strong lasers. *Comput. Phys. Commun.* **2023**, *290*, 108787. [CrossRef]
47. Fano, U. Propensity rules: An analytical approach. *Phys. Rev. A* **1985**, *32*, 617. [CrossRef]

48. Busto, D.; Vinbladh, J.; Zhong, S.-Y.; Isinger, M.; Nandi, S.; Maclot, S.; Johnsson, P.; Gisselbrecht, M.; L'Huillier, A.; Lindroth, E.; et al. Fano's Propensity Rule in Angle-Resolved Attosecond Pump-Probe Photoionization. *Phys. Rev. Lett.* **2019**, *123*, 133201. [CrossRef]
49. Chen, Z.; Morishita, T.; Le, A.T.; Wickenhauser, M.; Tong, X.-M.; Lin, C.-D. Analysis of two-dimensional photoelectron momentum spectra and the effect of the long-range Coulomb potential in single ionization of atoms by intense lasers. *Phys. Rev. A* **2006**, *74*, 053405. [CrossRef]